

See discussions, stats, and author profiles for this publication at: <https://www.researchgate.net/publication/229906479>

Accessible Volumes for Adsorption in Carbon Nanopores of Different Geometries and Wall Thicknesses

ARTICLE *in* THE JOURNAL OF PHYSICAL CHEMISTRY C · APRIL 2011

Impact Factor: 4.77 · DOI: 10.1021/jp202066w

CITATION

1

READS

20

3 AUTHORS, INCLUDING:



Jian Liu

Pacific Northwest National Laboratory

35 PUBLICATIONS 1,342 CITATIONS

SEE PROFILE



Duong Do

University of Queensland

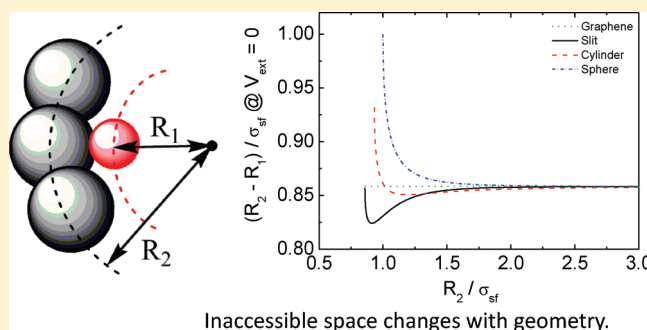
495 PUBLICATIONS 8,536 CITATIONS

SEE PROFILE

Accessible Volumes for Adsorption in Carbon Nanopores of Different Geometries and Wall Thicknesses

Jian Liu,[†] M. Douglas LeVan,^{*,†} and D. D. Do[‡][†]Department of Chemical and Biomolecular Engineering, Vanderbilt University, PMB 351604, Nashville, Tennessee 37235-1604, United States[‡]School of Chemical Engineering, University of Queensland, St. Lucia, QLD 4072, Australia

ABSTRACT: The accessible pore space for Lennard-Jones gas molecules adsorbed in smooth-walled carbon nanopores in the Henry's law region is determined for slit-shaped, cylindrical, and spherical pores. The size of this space, over which the total potential is nonpositive, depends on pore geometry and number of wall layers. Pores with small surface mean curvature are more accessible than those with larger surface mean curvature. Adding layers to the wall helps to increase the accessible pore space, but this effect is small after the second layer. Limits are determined for the smallest pores having accessible space. For the slit-shaped pore with a single wall, the minimum pore half width is the same as the width of the inaccessible layer at the wall of a single graphene sheet, which is less than the Lennard-Jones solid–fluid collision diameter. In contrast, the minimum radius of a spherical pore with accessible space is the Lennard-Jones solid–fluid collision diameter.



1. INTRODUCTION

The Henry's law constant of an adsorption isotherm and the isosteric heat of adsorption are important measures of gas adsorption affinity. Besides direct measurements and evaluation using isotherm data, theoretical calculations of Henry's law constants and isosteric heats of adsorption based on statistical thermodynamics are numerous.^{1–10} The selection of an appropriate pore volume and pore radius for the calculation of these properties is important. For example, the equation that Steele and others adopted to calculate the Henry's law constant is based on an absolute void volume, which causes the Henry's law constant at high temperatures to be negative. A negative Henry's law constant can be avoided by replacing the absolute void volume with an accessible pore volume.^{9,10}

Do et al.^{9,10} proposed that the outer boundary of the accessible pore volume be where the external wall potential is zero for Lennard-Jones (LJ) gas molecules in the limit of zero loading. The accessible void volume was then determined using Monte Carlo integration. Do and coauthors^{11–13} also defined an accessible pore size as the diameter of the largest sphere than can be put inside the accessible volume using a Tri-POD method. They pointed out that accessible pore radius and accessible pore volume vary for gas molecules with different LJ parameters.

In this paper, we adopt the definition of accessible pore volume of Do et al.^{9,10} and apply it to planar, cylindrical, and spherical geometries. We investigate the effects of pore radius or half width, pore geometry, and the number of carbon layers forming the pore wall on the accessible pore radius or half width. The results of our geometrical method can be easily

applied to estimate accessible pore volumes for LJ molecules adsorbed in a wide variety of carbon nanopores in the Henry's law region.

2. THEORY

Slit-shaped, cylindrical, and spherical single-wall carbon nanopore and graphene model potentials and parameters are taken from the literature.^{6,7,14,15} Gas molecules and carbon atoms are described by a single site model. The carbon atoms are assumed to be uniformly distributed over the wall with specific surface number densities. As in our previous papers,^{7,8} adsorbate–adsorbate interactions are neglected because of the infinitesimal gas concentration in the Henry's law region. The site-to-site interactions are described by the LJ potential. The LJ parameters and properties used in this paper are listed in Table 1. Averaged external wall potentials are obtained by integrating the pairwise LJ potential over the inner spaces of the pores to account for all carbon atoms for a flat plane, a slit-shaped pore, a cylindrical pore, and a spherical cavity.^{14,15}

For the various geometries, the distance between the centers of the carbon atoms on opposing walls of the pore will be referred to as pore diameter, and R is half of the pore diameter, i.e., the perpendicular distance from the center of a carbon atom to the center axis of the pore. ρ is the perpendicular distance from the center axis of the pore to the center of a fluid molecule.

Received: March 3, 2011

Revised: May 11, 2011

Published: May 13, 2011

Table 1. LJ Parameters and Surface Carbon Number Densities for Different Geometries

item	value	references
argon–carbon	$\sigma_{sf} = 3.35 \text{ \AA}$	6, 16
	$\epsilon_{sf}/k = 55.0 \text{ K}$	6, 16
carbon	layer spacing = 3.35 \AA	1, 6, 16
	n_s for sphere = $4.10 \times 10^{19} \text{ m}^{-2}$	7
	n_s for others = $3.82 \times 10^{19} \text{ m}^{-2}$	7, 17

We assume that adsorption occurs only on the internal surface of the pores, except for graphene which has adsorption on a single side. Furthermore, a small opening is assumed to exist into a spherical nanocavity; this allows gas molecules to pass through the cavity wall while having little effect on the overall solid–fluid potential.

For a planar graphene surface, the external wall potential is given by¹⁴

$$V_{\text{ext, graphene}} = 8\pi n_s \epsilon_{sf} \sigma_{sf}^2 \left[\frac{1}{10} \left(\frac{\sigma_{sf}}{R} \right)^{10} \left(1 - \frac{\rho}{R} \right)^{-10} - \frac{1}{4} \left(\frac{\sigma_{sf}}{R} \right)^4 \left(1 - \frac{\rho}{R} \right)^{-4} \right] \quad (1)$$

where n_s is the carbon number density (atoms per unit pore surface area). ϵ_{sf} and σ_{sf} are the solid–fluid well depth potential and the solid–fluid collision diameter and are often evaluated using the Lorentz–Berthelot mixing rules, i.e., $\epsilon_{sf} = (\epsilon_{ss}\epsilon_{ff})^{1/2}$ and $\sigma_{sf} = (\sigma_{ss} + \sigma_{ff})/2$. Equation 1 has been written using notation that allows easy comparison with pore geometries. For the graphene sheet, the normal distance of a gas molecule from the center of the plane of carbon atoms in the smoothed wall is $(R - \rho)$.

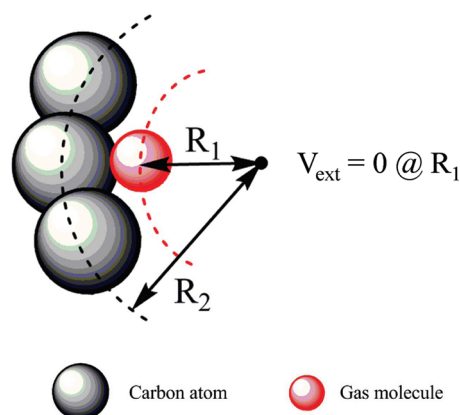
The remaining potentials are more complicated because of the effects of surrounding walls. For the parallel-sided slit-shaped pore, the external wall potential is given by^{7,14,18}

$$V_{\text{ext, slit}} = 8\pi n_s \epsilon_{sf} \sigma_{sf}^2 \left\{ \frac{1}{10} \left(\frac{\sigma_{sf}}{R} \right)^{10} \left[\left(1 - \frac{\rho}{R} \right)^{-10} + \left(1 + \frac{\rho}{R} \right)^{-10} \right] - \frac{1}{4} \left(\frac{\sigma_{sf}}{R} \right)^4 \left[\left(1 - \frac{\rho}{R} \right)^{-4} + \left(1 + \frac{\rho}{R} \right)^{-4} \right] \right\} \quad (2)$$

Similarly, for cylindrical geometry, we have^{10,14}

$$V_{\text{ext, cyl}} = n_s \pi^2 \epsilon_{sf} \sigma_{sf}^2 \left\{ \frac{63}{32} \left[\frac{R - \rho}{\sigma_{sf}} \left(1 + \frac{\rho}{R} \right) \right]^{-10} F \left[-\frac{9}{2}, -\frac{9}{2}; 1; \left(\frac{\rho}{R} \right)^2 \right] - 3 \left[\frac{R - \rho}{\sigma_{sf}} \left(1 + \frac{\rho}{R} \right) \right]^{-4} F \left[-\frac{3}{2}, -\frac{3}{2}; 1; \left(\frac{\rho}{R} \right)^2 \right] \right\} \quad (3)$$

where $F[\alpha, \beta; \gamma; z]$ is the hypergeometric series with parameters α , β , and γ .¹⁹ Finally, for a spherical surface, the external wall

**Figure 1.** Schematic for definition of accessible pore radius.

potential is¹⁵

$$V_{\text{ext, sph}} = 8\pi R^2 n_s \epsilon_{sf} \left[- \left(\frac{\sigma_{sf}}{R} \right)^6 \frac{1}{4(\rho/R)} \left(\frac{1}{(1 - \rho/R)^4} - \frac{1}{(1 + \rho/R)^4} \right) + \left(\frac{\sigma_{sf}}{R} \right)^{12} \frac{1}{10(\rho/R)} \left(\frac{1}{(1 - \rho/R)^{10}} - \frac{1}{(1 + \rho/R)^{10}} \right) \right] \quad (4)$$

Equations 2–4 are external wall potentials for single-wall carbon nanopores with different geometries. To obtain the external wall potentials for multiwall carbon surfaces, following Steele^{20,21} and others,^{10,22–24} we sum the single wall potentials layer by layer as described in our previous paper.⁸ Thus, the external wall potentials, whether they are for a wall with a single carbon layer or several layers, are obtained by adding together all two-body interactions between a gas molecule and all carbon atoms. Finally, limiting values for the infinite layer wall are obtained when the inclusion of additional layers has no effect on results to the accuracy shown. Thus, the external wall potential will depend both on curvature effects as given by the geometry (i.e., eqs 1–4) and on the number of layers included in the summation for the wall.

Following Do et al.,^{11,12} the accessible pore radius is defined as the distance between the center of a pore and the center of a gas molecule located where the external wall potential is zero. Our notation is shown in Figure 1. R_2 is the pore radius, or the distance from the center of the pore to the center of carbon atom on the wall. R_1 is the accessible pore radius, or the distance from the center of the pore to the center of a gas molecule located where the external wall potential is zero.

Our calculations are based on argon. Similar calculations can be performed for other probe molecules.

3. RESULTS AND DISCUSSION

3.1. Accessible Pore Space for Pores with Single-Layer Walls. The accessible pore half width or radius for argon adsorbed on graphene and in pores with single-layer walls of slit-shaped, cylindrical, and spherical geometries were obtained by determining the location where external wall potentials are zero. To solve eqs 1–4, ρ and R are set to R_1 and R_2 , respectively.

Figure 2 shows the width of the inaccessible space next to the wall for a graphene layer and for single-walled pores of the three geometries. Results are plotted in a dimensionless way by nor-

malizing with respect to the solid–fluid collision diameter. The x axis is the dimensionless pore radius. The y axis is the dimensionless difference between the pore radius and the accessible pore radius or, equivalently, the dimensionless thickness of the inaccessible pore space at the pore wall. This variable indicates how close the center of a gas molecule can approach the center of a carbon atom. As shown in Figure 2, the dimensionless inaccessible space for graphene is constant, always 0.8584, which can be determined from the external wall potential for the graphene, eq 1. Do et al.²⁴ first reported zero positions for gas adsorbed on flat surfaces with single and multilayer walls. The zero potential position was found at $0.8584\sigma_{sf}$ for a flat surface with a single layer wall. We will use the symbol Δ_g throughout the remainder of this paper to represent the dimensionless width of the inaccessible layer at the wall of a single graphene sheet, i.e., 0.8584.

Note that for a gas molecule interacting with a single carbon atom, the zero potential position occurs at $R_2 - R_1 = \sigma_{sf}$ i.e., at a dimensionless inaccessible pore space of unity. For the graphene sheet, this position is closer to the wall, at Δ_g . This results from the repulsion of the gas molecule by the closest carbon atoms in the graphene sheet being exactly balanced by attraction of the gas molecule by carbon atoms farther away in the graphene sheet.

For the three pore geometries shown in Figure 2, the inaccessible pore space approaches Δ_g asymptotically as the pore size increases. In this limit, the pore sizes become so large that the differences in surface curvatures for the different geometries disappear and the gas molecule is effectively interacting with a single planar wall. Thus, all systems approach the behavior of the single graphene sheet at very large radii.

The slit-shaped carbon pore with single layer walls is composed of two parallel planes of graphene. In contrast to the results for a single layer of graphene, the inaccessible space for the slit-shaped pore has a minimum in the inaccessible pore space as

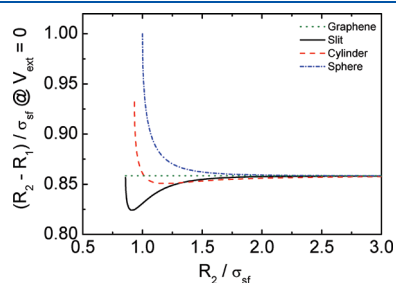


Figure 2. Inaccessible pore space for Ar adsorbed on graphene and in pores with slit-shaped, cylindrical, and spherical geometries as a function of pore diameter.

shown in Figure 2. This minimum is $(R_2 - R_1)/\sigma_{sf} = 0.8242$ and occurs at a dimensionless pore radius of 0.9157. This minimum can be explained by a superposition effect involving the two walls as illustrated in Figure 3. The pores have two walls, wall A and wall B, as indicated by vertical lines. We first consider the gas molecule to be closer to wall A. Again, the interaction potential between the carbon atoms of the wall and the gas molecule is an integrated LJ potential which is composed of two parts, an attractive potential and a repulsive potential. The attractive potential acts over a longer range than the steeper repulsive potential. As shown in the first diagram of Figure 3, with the walls far apart and the gas molecule close to wall A, the carbon atoms on wall B have no significant effect and the gas molecule can penetrate into the carbon wall to a position where the repulsive potential is balanced by the attractive potential giving the dimensionless inaccessible pore space of Δ_g of the single graphene sheet. As the pore width decreases further, with wall B moving toward wall A as shown in the second diagram of Figure 3, the net potential between the gas molecule and wall B becomes attractive and this can be balanced by a net repulsive potential between the gas molecule and wall A in order for the total potential determining accessibility to be zero. Thus, the gas molecule at the zero potential boundary will be closer to wall A than it is in the first diagram. This explains the decrease in the dimensionless inaccessible pore space of the slit-shaped pore from the large pore asymptote. As wall B continues to approach wall A, as shown in the third diagram of Figure 3, a limit is reached for the zero potential surface to exist in the pore. Interestingly, this occurs at the inaccessible pore space distance of Δ_g on each wall that was found for the single graphene sheet. At this location, attractive and repulsive potentials between the gas molecule and each of the walls are in perfect balance. If the gas molecule were to move toward either wall, then the net repulsive potential with that wall would be greater than the net attractive potential with the other wall because of the steepness of the LJ repulsive potential. Thus, the inaccessible space at a pore wall of the smallest accessible slit-shaped pore is identical to the inaccessible space adjoining the graphene sheet. The curve for the single-walled slit-shaped pore begins and ends at $(R_2 - R_1)/\sigma_{sf} = \Delta_g$.

The results for cylindrical and spherical pores are different from that of the slit-shaped pore as shown in Figure 2. The curve for the cylindrical pore has a shallower and broader minimum than the slit-shaped pore, and the curve for the spherical pore does not even have a minimum. These results can be ascribed to the different surface mean curvatures of the various carbon nanopores. Obviously, the spherical surface has the largest mean

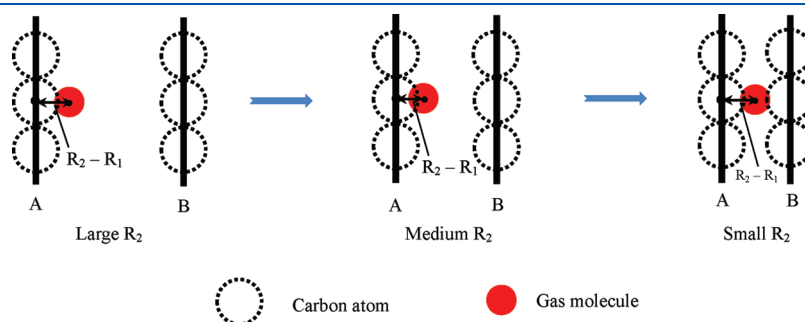


Figure 3. Effect of reducing pore radius on accessible volume for slit-shaped pores: left, walls far apart, $(R_2 - R_1)/\sigma_{sf} = \Delta_g$; middle, wall B attracting, $(R_2 - R_1)/\sigma_{sf} < \Delta_g$; right, tightest accessible pore, $(R_2 - R_1)/\sigma_{sf} = \Delta_g$.

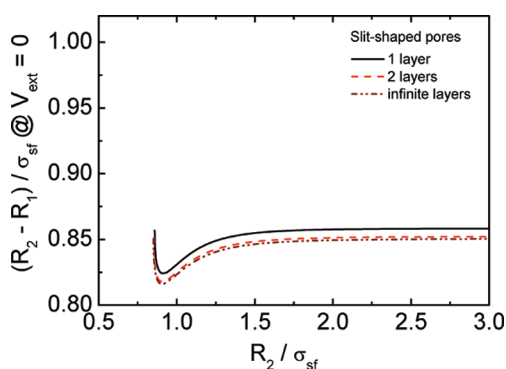


Figure 4. Inaccessible pore space for slit-shaped pores with multi-layered walls.

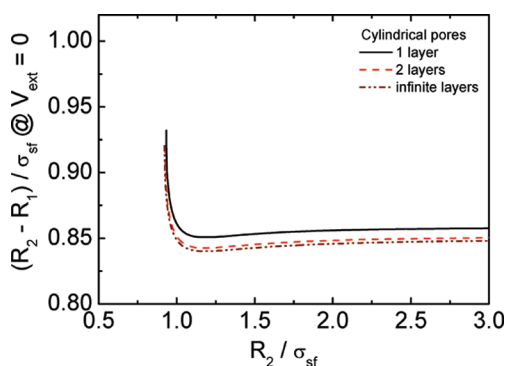


Figure 5. Inaccessible pore space for cylindrical pores with multi-layered walls.

curvature among the three geometries given the same pore radius. As is apparent from Figure 1, for a fixed pore dimension, a larger surface mean curvature gives a larger number of carbon atoms close to the gas molecule that influence it strongly in three-dimensional space.²⁵ Therefore, when the pore radius decreases from a middle range to a small value for a cylindrical pore, in comparison to the slit-shaped pore a larger number of carbon atoms are present nearby to contribute to the repulsive potential at a relatively larger pore dimension. The minimum then, which balances the net attractive and repulsive potentials, occurs at a larger pore dimension than for the slit-shaped pore. In addition, the curve for the cylindrical pore increases sharply when the dimensionless pore radius is less than unity, because the number of carbon atoms that contribute repulsive potentials increases sharply when the pore radius is smaller than σ_{sf} . Similarly, the dimensionless inaccessible pore space continues to increase with a decrease in pore size for the cylindrical pore until it terminates at $R_2/\sigma_{sf} = 1.0727$, where $(R_2 - R_1)/\sigma_{sf} = 0.9312$ with the zero potential surface being simply the pore axis.

The spherical pore has an even larger surface mean curvature than the cylindrical pore. As shown in Figure 2, no minimum is found for the inaccessible pore space. As the size of this spherical nanocavity shrinks, the width of this space increases rapidly. The curve terminates at $R_2/\sigma_{sf} = 1$ at which point $(R_2 - R_1)/\sigma_{sf} = 1$. At that point, the gas molecule is at zero potential at the center of the spherical cavity. The attractive and repulsive potentials are balanced for interaction with each individual carbon atom forming the spherical nanocavity. The distance of the gas molecule from the wall is exactly that given by the LJ potential

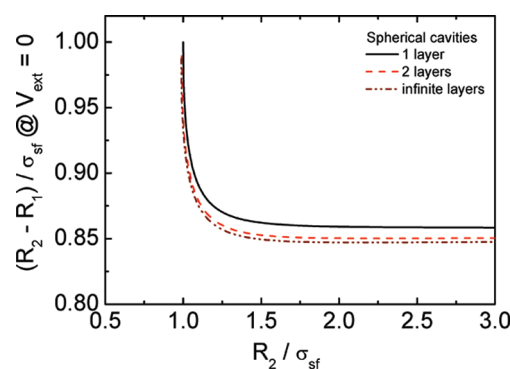


Figure 6. Inaccessible pore space for spherical pores with multi-layered walls.

Table 2. Limiting Dimensionless Inaccessible Pore Spaces for Pores with Different Geometries and Numbers of Wall Layers^a

layers of wall	slit-shaped pore		cylindrical pore		spherical pore	
	min	max	min	max	min	max
1	0.8242	0.8584	0.8508	0.9312	0.8584	1.0000
2	0.8179	0.8522	0.8426	0.9232	0.8502	0.9894
3	0.8168	0.8512	0.8411	0.9204	0.8484	0.9861
4	0.8164	0.8508	0.8405	0.9188	0.8478	0.9847
∞	0.8161	0.8506	0.8401	0.9187	0.8471	0.9836

^a Values are $(R_2 - R_1)/\sigma_{sf}$.

at zero potential for the interaction of the gas molecule with a single carbon atom. The spherical pore has the largest width of inaccessible pore space followed by the cylindrical pore and then the slit-shaped pore.

3.2. Effect of Number of Wall Layers on the Accessible Pore Space. In addition to considering pores with single-layer walls, accessible pore spaces were also investigated for pores with multilayer walls. As mentioned previously, for this case, the position of the zero external wall potential depends also on the spacing between carbon layers.

Results for multilayer slit-shaped, cylindrical, and spherical pores are shown in Figures 4, 5, and 6. Pores with multilayer walls have smaller inaccessible pore spaces compared with pores with single layer walls at fixed pore sizes. This is a result of attraction between the gas molecule and carbon atoms in layers beyond the first. Net attractive and repulsive potentials are in balance with the gas molecule being closer to the pore wall. However, layers beyond the second do not cause significant changes in the results. For a particular geometry, curves for pores with two or more layers give almost the same results. This is consistent with a prior result of Do et al.²⁴ for slit-shaped pores, who also found that the zero position depends on the ratio of the distance between carbon layers to σ_{sf} .

Values of maximum and minimum inaccessible pore spaces for pores with different geometries and numbers of wall layers are summarized in Table 2. It is clear that the difference in the maximum and minimum dimensionless inaccessible pore widths between consecutive layers decreases with increasing numbers of layers, as would be expected. For a fixed size pore, the spherical pore has the largest dimensionless inaccessible pore width

followed by the cylindrical and slit-shaped pores. The results shows that, for the same R_2 , pores with slit-shaped geometry are more accessible than those with cylindrical and spherical geometries.

For pores with slit-shaped and cylindrical geometries, the minimum in the curve for inaccessible pore space occurs at approximately the same value of R_2 for pores with single and multilayer walls. Although the effect is slight and not readily apparent in Figure 6, spherical pores with multilayer walls have very shallow minima, in contrast to the single wall spherical pores which showed no minimum. The outer shells, being curved less than the first shell, help to balance attractive and repulsive forces for a molecule closer to the wall. Evidence of this effect is found further in the termination of the curves at values of R_2/σ_{sf} slightly less than unity.

4. CONCLUSIONS

A geometric method was used to study accessible pore space as a function of pore dimension for slit-shaped, cylindrical, and spherical carbon pores in the Henry's law region. Pore walls with single layers and multiple layers of carbon were considered.

The inaccessible pore space at the pore wall was found to depend on both pore geometry and number of wall layers. Surface mean curvature was found to be quite important in determining the relationship between the accessible pore space and the pore dimension when the pore size is comparable to the size of the adsorbate. In general, pores with small surface mean curvature are more accessible to a gas molecule than those with larger surface mean curvature given the same characteristic pore dimension. Slit-shaped pores have less inaccessible pore space at the wall than cylindrical pores, which have less inaccessible space than spherical pores. Pores with multilayer walls have less inaccessible pore space than pores with a single wall. Adding layers to the wall helps to increase the size of the accessible pore space, but this effect is quite small after the second layer for pores of all three geometries.

For very large pores with a single-layer wall, the dimensionless accessible pore space is not sensitive to the pore radius and a universal limit for the width of the inaccessible pore space exists for the different geometries because of the diminishing surface mean curvatures of the geometries. In this limit, all pores behave like a single sheet of graphene.

Limits were determined for the smallest pores having accessible space. For the slit-shaped pore with a single wall, the minimum pore half-width is $0.8584\sigma_{sf}$ which is also the width of the inaccessible layer at the wall for a single graphene sheet. In contrast, the minimum radius of a spherical pore with accessible space is σ_{sf} the Lennard-Jones collision diameter.

AUTHOR INFORMATION

Corresponding Author

*E-mail: m.douglas.levan@vanderbilt.edu (M. D. LeVan).

REFERENCES

- (1) Steele, W. A. *The Interaction of Gases with Solid Surfaces*; Pergamon Press: Oxford, 1974.
- (2) Everett, D. H.; Powl, J. C. *J. Chem. Soc., Faraday Trans. 1* **1976**, 72, 619–636.
- (3) Vernov, A.; Steele, W. A. *Langmuir* **1991**, 7, 3110–3117.
- (4) Floess, J. K.; Vanlshout, Y. *Carbon* **1992**, 30, 967–973.

- (5) Pikunic, J.; Clinard, C.; Cohaut, N.; Gubbins, K. E.; Guet, J.; Pellenq, J. M.; Rannou, L.; Rouzaud, J. N. *Langmuir* **2003**, 19, 8565–8582.
- (6) Schindler, B. J.; LeVan, M. D. *Carbon* **2008**, 46, 644–648.
- (7) Liu, J.; LeVan, M. D. *Carbon* **2009**, 47, 3415–3423.
- (8) Liu, J.; LeVan, M. D. *Carbon* **2010**, 48, 3454–3462.
- (9) Do, D. D.; Nicholson, D.; Do, D. H. *J. Colloid Interface Sci.* **2008**, 324, 15–24.
- (10) Do, D. D.; Do, H. D.; Wongkoblap, A.; Nicholson, D. *Phys. Chem. Chem. Phys.* **2008**, 10, 7293–7303.
- (11) Do, D. D.; Herrera, L. F.; Do, D. H. *J. Colloid Interface Sci.* **2008**, 328, 110–119.
- (12) Do, D. D.; Herrera, L. F.; Fan, C. Y.; Wongkoblap, A.; Nicholson, D. *Adsorption* **2010**, 16, 3–15.
- (13) Herrera, L.; Fan, C. Y.; Do, D. D.; Nicholson, D. *Adsorption* **2011**, 17, 55–68.
- (14) Tjatjopoulos, G. J.; Feke, D. L.; Adin Mann, J., Jr. *J. Phys. Chem.* **1988**, 92, 4006–4007.
- (15) Baksh, M. S. A.; Yang, R. T. *AIChE J.* **1991**, 37, 923–930.
- (16) Ravikovitch, P. I.; Nishnyakov, A.; Russo, R.; Neimark, A. V. *Langmuir* **2000**, 16, 2311–2320.
- (17) Do, D. D. *Adsorption Analysis: Equilibria and Kinetics*; Imperial College Press: London, 1998.
- (18) Bandosz, T. J.; Biggs, M. J.; Gubbins, K. E.; Hattori, Y.; Iiyama, T.; Kaneko, K.; Pikunic, J.; Thomson, K. T. *Chem. Phys. Carbon* **2003**, 28, 41–228.
- (19) Gradshteyn, I. S.; Ryzhik, I. M. *Table of Integrals, Series, and Products*; Academic Press: New York, 1980.
- (20) Steele, W. A. *Surf. Sci.* **1973**, 36, 317–352.
- (21) Steele, W. A. *Chem. Rev.* **1993**, 93, 2355–2376.
- (22) Do, D. D.; Do, D. H. *J. Phys. Chem. B* **2006**, 110, 9520–9528.
- (23) Fischer, J. *Fluids at Interfaces. Molecular Based Study of Fluids*; Advances in Chemistry Series 204; American Chemical Society: Washington, DC, 1983; Chapter 6.
- (24) Do, D. D.; Do, D. H. *J. Colloid Interface Sci.* **2007**, 316, 317–330.
- (25) Jiang, J. W.; Wagner, N. J.; Sandler, S. I. *Phys. Chem. Chem. Phys.* **2004**, 6, 4440–4444.